

# Chiral smectic $A$ membranes: Unified theory of free edge structure and twist walls

C. Nadir Kaplan<sup>\*†</sup> and Robert B. Meyer

*The Martin Fisher School of Physics, Brandeis University, Waltham, Massachusetts 02454*

(Dated: December 3, 2024)

Monodisperse suspensions of rodlike chiral  $fd$  viruses are condensed into a rod-length thick colloidal monolayers of aligned rods by depletion forces. Twist deformations of the molecules are expelled to the monolayer edge as in a chiral smectic  $A$  liquid crystal, and a cholesteric band forms at the edge. Coalescence of two such isolated membranes results in a twist wall sandwiched between two regions of aligned rods, dubbed  $\pi$ -walls. Based on the analogy of smectics  $A$  with superconductors, we develop a unified theory of the  $\pi$ -walls and the monolayer edge. The mean-field analysis of our model yields the molecular tilt profiles, the local thickness change, and the crossover from smectic-to-cholesteric behavior at the monolayer edge and across the  $\pi$ -wall. Furthermore, we calculate the line tension associated with the formation of these interfaces. Our model offers insights regarding the stability and the detailed structure of the  $\pi$ -wall and the monolayer edge.

## I. INTRODUCTION

Chirality, the breaking of mirror symmetry, occurs at many length scales, from nanometer-sized DNA to the coiled form of Gastropod snails at various sizes [1]. In soft matter, microscopic chirality can alter numerous macroscopic properties of materials. For example, in chiral smectic liquid crystals grain boundaries form above a critical temperature to alleviate the frustration between the layer formation and the twist tendency of the chiral molecules [2–4]. This is analogous to the penetration of magnetic field lines into superconductors by creating a lattice of parallel vortices [5]. Based on this analogy, smectic  $A$  samples maintain twist- and bend-free molecular orientations within each layer by the expulsion of these deformations to the edges or around isolated defects, similar to the well-known Meissner effect in superconductors [6].

One realization of this analogy is a model system of two dimensional colloidal membranes composed of aligned rods, which behave as a single layer of a chiral smectic  $A$  ( $Sm-A^*$ ) liquid crystal. Monodisperse suspensions of the 880 nm long, rodlike wild-type  $fd$  viruses are spontaneously condensed into these one rod length thick colloidal monolayers with free edges by attractive depletion forces [7–9]. The penetration of twist at the monolayer edge could be directly observed, allowing for the confirmation of the de Gennes theory [10]. Recently, it was reported that the line tension of the monolayer edge, an important variable relevant to the formation energy of the free boundaries, can be controlled *in situ* by the chirality of rods [11]. Furthermore, it was found that monolayers which consist of achiral rods still possessed twist deformations at the edge. A curved edge profile was observed, which was robust for the entire range of measured line tension values.

By changing the line tension, colloidal  $Sm-A^*$  membranes can easily be induced to exhibit morphological transitions [11]. One way to achieve this is the coalescence of two or more membranes. When two membranes are surrounded by the edges with same handedness, the molecular twist localized at the edge poses a problem for the coalescence, as the direction of twist will be in opposite directions where the two edges meet. The final structure adopts a one-dimensional line defect between the two coalesced membranes when the sizes of the two membranes are comparable to each other. In order for the molecular arrangement across the defect to be continuous, the rods must twist by  $\pi$  radians. Henceforth we will refer to these lines of twist as  $\pi$ -walls. These can also be imprinted in the monolayers using optical forces [12].

In this paper we propose a unified theory of the monolayer edge and the  $\pi$ -walls based on the Landau-Ginzburg formalism of smectics, which was put forward by de Gennes [6]. The de Gennes framework couples the smectic order within the monolayer and the orientation of the nematic director field of the constituent molecules for small elastic distortions. In the present work, the effect of the depleting agent, *i.e.* the nonadsorbing polymer, is modeled by appropriate surface tension terms, and plays a crucial role in determining the structure of the monolayer edge and the  $\pi$ -walls. We perform a mean-field analysis of our model to reproduce their shape, as well as revealing the tilt angle profiles of the molecules and the  $Sm-A^*$ -to- $Ch$  transition. Furthermore, we calculate the line tension of the membrane edge and the  $\pi$ -wall as a function of the molecular chirality, or equivalently temperature [11], in order to match them with experimental measurements. Accordingly, we investigate the thermodynamic stability of these structures with respect to each other.

$\pi$ -walls resemble various other phenomena observed in condensed matter systems. For instance, they are analogous to a laminar model of an array of alternating normal metal and superconducting regions, which was replaced by the Abrikosov flux-lattice phase in type-II materials [5, 13, 14]. Furthermore, the pitch associated with the helicity of a cholesteric sample can be unwound by

<sup>1</sup> \* E-mail: [nadir@seas.harvard.edu](mailto:nadir@seas.harvard.edu)

<sup>2</sup> † Present address: *School of Engineering and Applied Sciences, Harvard University, Cambridge, Massachusetts 02138, USA.*

electric and magnetic fields, creating similar twist walls in the vicinity of the critical field [15, 16]. Another example is magnetic systems, where the rotation of spin magnetic moments in space cause resembling domains called Bloch walls [17].

The present study is organized as follows: In the next section, based on experimental evidence, we explain the hypothesized structures of the membrane edge and the  $\pi$ -wall followed by a detailed description of our model. In section III we present the results, where we apply our theory to the membrane edge and the  $\pi$ -wall in order to test our hypotheses. In addition, we calculate their line tension as a function of temperature and discuss the relative thermodynamic stability of the  $\pi$ -walls with respect to the monolayer edge. Concluding remarks are offered in the final section of the paper.

## II. THEORY

### A. Structures of the $\pi$ -wall and the monolayer edge

Disk-shaped assemblages of *fd*-viruses typically reach mesoscopic sizes in diameter [7]. Because of the tendency of monodisperse hard rods to build a one-rod-length thick flat monolayer, Sm- $A^*$  membranes do not support molecular twist and bend deformations and thus expel them to the edge (Figs. 1a, 1b) [18]. In general, bend deformations of the molecules are negligible as the rod length is much smaller than the monolayer radius. Since the rods are perfectly aligned in the bulk, the membrane interior appears black when viewed under 2D LC-Polscope, corresponding to no birefringence (Fig. 1c) [10, 11]. Towards the edge, however, optical anisotropy arising from the twist deformations results in a bright, birefringent region characterized by a retardance,  $R$ , which is given by (Fig. 1d)

$$R = t\Delta n_{sat}cS \sin^2 \theta. \quad (1)$$

Here  $t$  is the local membrane thickness.  $n_{Sat} = (3.8 \pm 0.3) \times 10^{-5}$  mL/mg is the specific birefringence of a fully aligned bulk sample at unit concentration [19]. The nematic order parameter  $S$  was measured to be 0.95 at a rod concentration  $c$  of 100 mg/mL in the bulk monolayer [19]. Therefore we assume that  $S \sim 1$ , namely there is perfect orientational order [7, 10].  $\theta$  is the tilt angle of the molecules with respect to the layer normal, as will be discussed below in detail.

To quantify the retardance, a simple model focusing on the spatial variation of the nematic director was proposed [10]. This model neglects the variation of the thickness and smectic order across the monolayer. For chiral membranes, the theory accurately reproduces the experimental retardance profile. However, the retardance map of achiral monolayers exhibits twist as well, spontaneously breaking the chiral symmetry at the membrane edge [11]. Furthermore, electron micrographs of

the membrane edge cross-section reveal a curved thickness profile and melting of the smectic order into a narrow cholesteric (chiral nematic –  $Ch$ ) band at the edge. In Fig. 1e, the rods are seen to be perfectly aligned in the  $z$ -direction in the bulk of the monolayer. Towards the edge, the rods tilt rapidly such that they point perpendicular to the image plane, forming a  $Ch$  region with a hemi-toroidal curved shape at the edge.

This  $Ch$  band constitutes the core of the  $\pi$ -wall as well, since a  $\pi$ -wall is formed from two free edges of same handedness (Fig. 2a). Therefore, we model the  $\pi$ -wall by a  $Ch$  region sandwiched between two semi-infinite Sm- $A^*$  monolayers (Figs. 2c, 2d).  $\pi$ -walls are linear defects, thereby their liquid crystalline order does not possess any bend deformations. As for their shape, the effect of the thickness variation is anticipated to be more prominent at the  $\pi$ -walls: an intensity profile having a local minimum located between two peaks is extracted from retardance measurements (Figs. 2b, 2e). We hypothesize that this local minimum indicates a significant variation of the membrane thickness across the  $\pi$ -wall.

The presence of the depleting agent results in an effective surface tension over the membrane surface. When a single molecule protrudes from the monolayer, it reduces the accessible volume of the surrounding depletant polymer. Both in experiments and simulations, it was found that protrusion fluctuations are significant in Sm- $A^*$  membranes, and stabilize this phase against the configuration where single disks stack up on top of each other and form a Sm- $A^*$  structure [7, 8, 26]. In addition, spontaneous twist at the edge of achiral monolayers is understood as an outcome of the surface tension: compared to an untilted edge configuration, the monolayer may reduce the rod-polymer interfacial area despite resulting in an elastic energy associated with twist deformations [11]. This configuration lowers the total surface energy of the membrane, especially if the surface tension continuously varies throughout the monolayer and becomes bigger at the edge than in the bulk, due to the changing rod orientation. This scenario will be discussed below. Hence, a curved edge shape is favored when surface tension becomes dominant in determining the structure of the monolayer edge. In previous theories, the thickness variation, as well as the  $Ch$ -band formation, were not taken into account, resulting in a line tension which is low by an order of magnitude in comparison to experimental results [20, 21].

### B. The unified free energy

These recent experimental findings are beyond the scope of the simple model proposed in Ref. [10]. Thus, in addition to the spatial change of the molecular tilt, a detailed theory should account for the local thickness variation and the crossover from Sm- $A^*$ -to- $Ch$  behavior across the monolayer and the  $\pi$ -wall, in order to correctly predict their structure as well as the magnitude and the

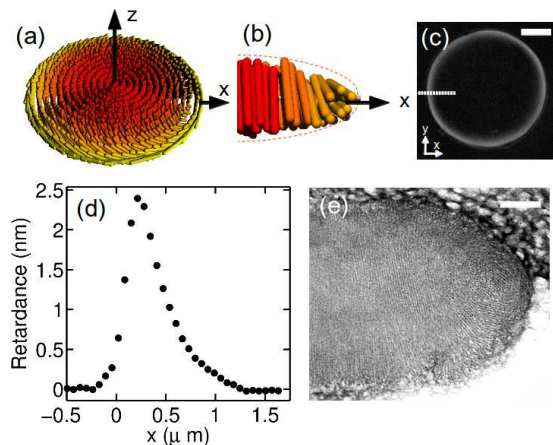


FIG. 1. **Structure of the membrane edge.** (a) The schematics of the rod orientation in a membrane and (b) at its edge [11]. (c) Retardance image of a membrane (top view) [10]. Black region corresponds to no retardance, whereas the bright ring at the edge is birefringent. (d) Radial retardance profile as a function of distance from the membrane edge (on the white dotted line shown in (c)) [10]. (e) Electron micrograph of the cross-section of the membrane edge [11]. It visualizes both the curved shape and the Sm- $A^*$ -to- $Ch$  transition towards the edge. Scale bars,  $5 \mu\text{m}$  (c);  $0.2 \mu\text{m}$  (e).

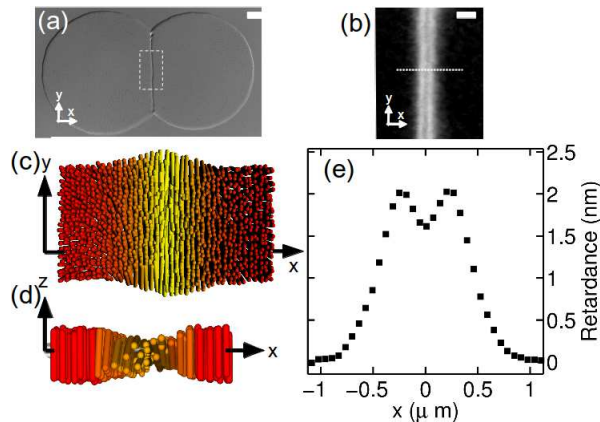


FIG. 2. **Structure of a  $\pi$ -wall [12].** (a) Two coalesced monolayers generate a  $\pi$ -wall in between. (b) Retardance image of a  $\pi$ -wall, showing a narrow black band at the center surrounded by a bright region. Schematics of the  $\pi$ -wall; (c) top view, (d) side view. (e) Retardance profile versus distance from the  $\pi$ -wall (on the white dotted line shown in (b)). The narrow black region in (b) corresponds to a local minimum at the center. Scale bars,  $3 \mu\text{m}$  (a);  $1 \mu\text{m}$  (b).

behavior of the line tension.

Our model is based on the de Gennes free energy for the  $Ch$ -Sm- $A^*$  transition [2, 6, 18]. The free energy per unit length of the Sm- $A^*$  flat layer in  $(x, y)$ -plane is given

by

$$F = \int dx t \left[ f_{Ch-A} + \frac{C_t}{2} \Psi^2 (t^2 - (t_0 \cos \theta)^2)^2 - \nu \right] + \oint ds \left( \sigma_{\parallel} (\hat{\mathbf{N}} \cdot \mathbf{n})^2 + \sigma_{\perp} (\hat{\mathbf{N}} \times \mathbf{n})^2 + k\kappa_c^2 \right). \quad (2)$$

The volume terms given in square brackets are multiplied by the local monolayer thickness  $t(x)$ .  $f_{Ch-A}$  in Eq. (2) is written as

$$f_{Ch-A} = -\frac{r}{2} \Psi^2 + \frac{u}{4} \Psi^4 + \frac{C_1}{2} (\nabla \Psi)^2 + \frac{C_2}{2} (\Psi \sin \theta)^2 + \frac{K_2}{2} (\mathbf{n} \cdot \nabla \times \mathbf{n} - q_0)^2, \quad (3)$$

which is the de Gennes free energy density for the  $Ch$ -Sm- $A^*$  transition due to *big* distortions of the nematic director in a flat smectic monolayer [10, 21]. In Eqs. (2) and (3),  $\Psi$  is the real part of the complex smectic order parameter  $\tilde{\Psi}$ . As in a conventional Sm- $A^*$  phase, the first three terms in Eq. (3) describe the transition from one rod-length thick monolayer of perfectly aligned  $fd$  ( $\Psi = \Psi_0 = \sqrt{\frac{r}{u}}$ ) to the  $Ch$  region forming at the monolayer edge and around the  $\pi$  wall ( $\Psi = 0$ ). The change in the phase of  $\tilde{\Psi}$  due to big distortions of the nematic director  $\mathbf{n}$  and arising from  $t \neq \cos \theta$  towards the  $\pi$  wall and the edge is absorbed in the second term of Eq. (2) and in the fourth term of Eq. (3) without loss of generality, ensuring rotational invariance. The fourth term in Eq. (3), which describes the energy cost of  $\mathbf{n}$  distorting perfect layer formation, exhibits a nonlinear dependence on the tilt angle. This term has no counterpart in superconductors. The last term of Eq. (3) represents the twist deformations, where  $K_2$  is the twist elastic modulus. It is the only contribution to  $f_{Ch-A}$  from the Frank free energy density, as the nematic director  $\mathbf{n} \equiv (0, \sin \theta(x), \cos \theta(x))$  rotates by an angle  $\theta$  about the  $x$ -axis within a characteristic length scale  $\lambda_t \equiv \sqrt{\frac{K_2}{C_2 \Psi_0^2}}$ , the twist penetration depth [10, 18]. Furthermore, the second term in Eq. (2) dictates that  $t = t_0$  (see Figs. 3a, 3b) in the region of fully aligned  $fd$  viruses ( $\Psi = \Psi_0$ ), and  $t$  is decoupled from the orientation of  $\mathbf{n}$  at the  $Ch$  band ( $\Psi = 0$ ). The last volume term denoted by the Lagrange multiplier  $\nu$  is due to the volume constraint of the membrane, arising from the rigid nature of the rod-like  $fd$  viruses. That is, the overall monolayer volume stays constant, being independent of the local molecular orientation.

The effect of the depletant polymer is represented by surface tension terms given in the second line of Eq. (2). The coefficients in the fourth and fifth terms of Eq. (2) are the bulk surface tension  $\sigma_{\parallel}$  when  $\mathbf{n} \parallel \hat{\mathbf{N}}$ , and the  $\pi$ -wall or edge surface tension  $\sigma_{\perp}$  when  $\mathbf{n} \perp \hat{\mathbf{N}}$ ,  $\hat{\mathbf{N}} \equiv (-\sin \phi(x), 0, \cos \phi(x))$  being the local unit normal of the membrane curved surface.  $\phi = \tan^{-1} \frac{dt}{dx}$  is the angle between  $\hat{\mathbf{N}}$  and  $z$ -axis.  $ds$  is the infinitesimal arc length of the curved surface, and its projection onto the  $x$ -axis

is  $dx$  (Figs. 3a, 3b). In the presence of anisotropy ( $\sigma_{\parallel} \neq \sigma_{\perp}$ ), the local surface tension changes continuously due to the local tilt of  $\mathbf{n}$  between the two regimes. The last term in Eq. (2) is the curvature free energy cost of the surface [22], where  $k$  is the associated curvature modulus. Instead of using  $t(x)$  and its derivatives, it is preferable to parametrize the curvature by the derivative of  $\phi$  with respect to the infinitesimal arc length, that is  $\kappa_c \equiv \frac{d\phi}{ds}$ , where  $ds = \frac{dx}{\cos \phi}$  [22].

Plugging in the expressions for  $\mathbf{n}$ ,  $\hat{\mathbf{N}}$ , and  $\kappa_c$ , Eqs. (2) and (3) are rewritten as

$$F = \int_0^{\infty} dx \left[ t f_{Ch-A} + \frac{C_t}{2} t \Psi^2 (t^2 - t_0^2 \cos^2 \theta)^2 - \nu t + \frac{\sigma_{\perp}}{\cos \phi} - \Delta \cos^2 \theta \cos \phi + k \cos \phi \left( \frac{d\phi}{dx} \right)^2 + \mu \left( \tan \phi - \frac{dt}{dx} \right) \right], \quad (4)$$

where  $\Delta \equiv \sigma_{\perp} - \sigma_{\parallel}$ , and

$$f_{Ch-A} = -\frac{r}{2} \Psi^2 + \frac{u}{4} \Psi^4 + \frac{C_1}{2} \left( \frac{d\Psi}{dx} \right)^2 + \frac{C_2}{2} \Psi^2 \sin^2 \theta + \frac{K_2}{2} \left( \frac{d\theta}{dx} - q_0 \right)^2. \quad (5)$$

In Eq. (4), due to the parametrization of  $\hat{\mathbf{N}}$  and  $\kappa_c$  in terms of  $\phi$ , there is an extra constraint of  $\tan \phi = \frac{dt}{dx}$  multiplied by the Lagrange multiplier  $\mu = \mu(x)$ .

For one independent and several dependent variables, the Euler-Lagrange (EL) equations which minimize Eq. (4) are given by [23]

$$\frac{\partial f}{\partial g_i} = \frac{d}{dx} \frac{\partial f}{\partial g'_i} \quad (6)$$

where  $g_i \equiv \{\theta, \Psi, t, \phi\}$ ,  $g'_i \equiv \{\theta', \Psi', t', \phi'\}$ , and  $f = f(g_i, g'_i)$  is the free energy density given by  $F = \int dx f(g_i, g'_i)$ . Primes denote derivatives  $\frac{dg}{dx}$ . With the constraint given in the last term of Eq. (4), Eq. (6) contains eight coupled nonlinear first-order differential equations that are solved subject to eight boundary conditions. These eight equations are calculated as

$$u_1 \equiv \frac{\partial f}{\partial \theta'} = K_2 t (\theta' - q_0), \quad (7)$$

$$u_2 \equiv \frac{\partial f}{\partial \Psi'} = C_1 t \Psi', \quad (8)$$

$$t' = \tan \phi, \quad (9)$$

$$\kappa_c = \cos \phi \phi', \quad (10)$$

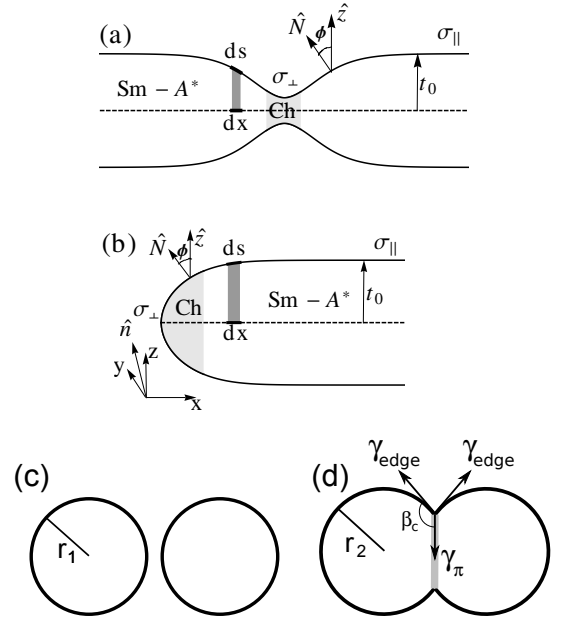


FIG. 3. **Schematics of the  $\pi$ -wall and the edge.** Side views of (a) the  $\pi$ -wall and (b) the edge. Dashed lines denote the mid-plane. Light-shaded area indicates the  $Ch$  region. Dark-shaded area indicates the projection of  $ds$ , which is  $dx$ . The surface normal  $\hat{\mathbf{N}}$  is in the  $(x, z)$ -plane.  $\phi$  is the angle between the  $z$ -axis and the surface normal  $\hat{\mathbf{N}}$ . The nematic director  $\mathbf{n}$  is always in the  $yz$ -plane. Schematics of (c) the two monolayers of radii  $r_1$  before coalescence and (d) the coalesced final structure with a  $\pi$ -wall (gray line). Each arc has the radius  $r_2$ . The line tensions  $\gamma_{edge}$  and  $\gamma_{\pi}$ , equivalent to the applied forces at the anchoring point, should be balanced in equilibrium.  $\beta_c$  is the contact angle. The relation  $r_2 \geq r_1$  always holds.

$$u'_1 = \sin 2\theta \left[ \Delta \cos \phi + t \Psi^2 \left( \frac{C_2}{2} - C_t t_0^4 \cos^2 \theta + C_t t_0^2 t^2 \right) \right], \quad (11)$$

$$u'_2 = t \Psi \left[ -r + C_2 \sin^2 \theta + C_t (t^2 - t_0^2 \cos^2 \theta)^2 + u \Psi^2 \right], \quad (12)$$

$$\mu' = \nu - \frac{\Psi^2}{2} \left[ -r + C_2 \sin^2 \theta + C_t t_0^4 \cos^4 \theta - 6C_t t_0^2 t^2 \cos^2 \theta + 5C_t t^4 \right] - \frac{u}{4} \Psi^4 - \frac{u_1^2}{2K_2 t^2} - \frac{u_2^2}{2C_1 t^2}, \quad (13)$$

$$2k \cos^2 \phi \kappa'_c = \Delta \cos^2 \theta \sin \theta \cos^2 \phi + \sigma_{\perp} \sin \phi + \mu - k \sin \phi \kappa_c^2. \quad (14)$$

The boundary conditions in the bulk are specified as follows: because there is parallel alignment of rods in the interior of the monolayer, no director tilt occurs ( $\theta_0 = 0$  or  $\theta_0 = \pi$ ), there is perfect smectic order ( $\Psi = \Psi_0$ ), and  $t = t_0$  (see Figs. 3a and 3b). The unit layer normal  $\hat{\mathbf{N}}$  is parallel to the  $z$ -axis, leading to  $\phi_0 = 0$ . Furthermore, all

derivatives must vanish in the bulk in the ground state of the monolayer.

Using the boundary conditions in the bulk, we determine the Lagrange multiplier of the volume constraint from Eq. (13) as

$$\nu = \frac{1}{2} \left( -\frac{r^2}{2u} + K_2 q_0^2 \right). \quad (15)$$

The physical meaning of  $\nu$  can be understood by the following argument: the volume difference between a configuration of uniformly aligned viruses parallel to the  $z$ -axis and the configuration shown in Fig. 1c contributes to the bulk of the monolayer by the associated energy density  $\nu$ , as the volume of the monolayer is constrained to stay constant in Eq. (2). The first term in Eq. (15) is the energy gain due to the Sm- $A^*$  order, and the second term is the energy cost of the chiral rods avoiding twist deformations.  $\nu$  vanishes at  $q_{0C} = \Psi_0^2 \sqrt{\frac{u}{2K_2}}$ , where  $q_{0C}$  is defined as the critical chirality.

For the  $\pi$ -wall and the monolayer edge structure, the boundary conditions are determined separately. The thickness of a  $\pi$ -wall saturates at a thickness  $t_\pi$  at the center, where  $\hat{\mathbf{N}}$  is parallel to the  $z$ -axis, hence  $\phi_\pi = 0$ . Since  $\pi$ -walls are modeled by a  $Ch$  region sandwiched between two Sm- $A^*$  monolayers,  $\Psi_\pi = 0$  and  $\theta_\pi = \frac{\pi}{2}$  by symmetry. As for the boundary conditions at the edge, from the electron micrograph (Fig. 1e), it is clear that  $\phi_{edge} = \frac{\pi}{2}$ , where  $t_{edge} = 0$ . Additionally, at the edge the viruses stay parallel to the  $y$ -axis along the membrane periphery, that is  $\theta_{edge} = \frac{\pi}{2}$ . We assume the rods forming a perfect  $Ch$  at the monolayer edge, thus  $\Psi_{edge} = 0$ .

The membrane edge and the  $\pi$ -wall show significant thermal fluctuations on the monolayer plane. The line tension  $\gamma_{eff}$ , which is the free energy cost associated with the formation of these interfaces, can be extracted from the analysis at the long wavelength limit of the measured fluctuation spectra [11, 12]. The magnitude of  $\gamma_{eff}$  is controlled by the chirality of the constituent rods, since the twist deformations expelled to the interface reduce the energy of rods arising from chiral interactions. The fluctuation amplitude is inversely proportional to  $\gamma_{eff}$ . The bigger the depletant concentration, the lower the fluctuation amplitude becomes at long wavelengths, leading to an increase in  $\gamma_{eff}$  [25]. Therefore it was proposed that the line tension is given by

$$\gamma_{eff} = \gamma_{bare} - \gamma_{chiral}, \quad (16)$$

where  $\gamma_{bare}$  depends on the depletant concentration, and  $\gamma_{chiral}$  is the chiral contribution to the line tension [11]. Theoretically,  $\gamma_{eff}$  can be calculated by [27]  $\gamma_{eff} = F - f_{mean}d$ , where  $F$  is given by Eq. (2),  $d$  is the width of the monolayer, and the mean free energy density of a large disk is written as  $f_{mean} = \nu + \sigma_{||}/t_0$ , since in Eq. (2) the contributions of twist deformations to  $f_{mean}$  are negligible [20, 21]. Rods present inside the

bulk create a surface energy associated with  $\sigma_{||}$ , which results in the second term of  $f_{mean}$ .

The configurations of two monolayers before and after coalescence are shown in Figs. 3(c) and 3(d). The coalesced form adopts a  $\pi$ -wall in between (gray line). The magnitudes of the forces applied to the anchor points by the  $\pi$ -wall and the monolayer edge are equal to the  $\gamma_\pi$  and  $\gamma_{edge}$ , the line tensions associated with the  $\pi$ -wall and the edge, respectively. In equilibrium these forces are balanced, giving rise to a certain contact angle  $\beta_c$ , which satisfies the relation

$$\gamma_\pi = -2\gamma_{edge} \cos \beta_c. \quad (17)$$

Eq. (17) ignores the detailed three dimensional (3D) structure of the anchor points and assumes that the forces are balanced on the monolayer plane. In reality, the forces may be balanced in a more sophisticated way, stemming from the 3D form of the anchor points. Experimentally it is predicted that these anchors build non-orientable surfaces [12]. Ignoring the detailed structure of the  $\pi$ -wall and the monolayer edge, we further assume that the total area of two monolayers is conserved. Namely,  $A_{1st} = A_{2nd}$ , where the  $A_{1st}$  and  $A_{2nd}$ , the total areas of the first and second configurations, respectively, are given by

$$A_{1st} = 2\pi r_1^2, \quad \text{and} \quad A_{2nd} = (2\beta_c - \sin 2\beta_c)r_2^2. \quad (18)$$

To determine the stability of  $\pi$ -walls with respect to the membrane edge, we compare the total line energies of the first and second configurations,  $F_{1st}$  and  $F_{2nd}$ , which are written as

$$F_{1st} = 4\pi r_1 \gamma_{edge}, \quad (19)$$

$$F_{2nd} = 4\beta_c r_2 \gamma_{edge} + 2r_2 \sin \beta_c \gamma_\pi. \quad (20)$$

When  $\Delta F \equiv F_{1st} - F_{2nd} > 0$  under the constraints given by Eqs. (17) and (18),  $\pi$ -walls should be favored. On the other hand, if  $\Delta F \leq 0$ , the  $\pi$ -wall length goes to zero as the two coalesced disks will separate into two distinct monolayers, namely back to the first configuration. At  $\Delta F = 0$ ,  $\beta_c$  becomes equal to  $\pi$ , implying a continuous transition between the two regimes. Hence, the region of  $\pi$ -wall stability is given as  $\beta_c < \pi$ . In this regime, the radius of a single arc in the second configuration,  $r_2$ , is always bigger than  $r_1$ , the radius of a single disk.

### III. RESULTS

#### A. Methods

We now explore the results by solving the EL Equations given in Eqs. (7)–(14) and their respective boundary conditions for the  $\pi$ -wall and the monolayer edge. Since

the EL Equations are coupled to each other and non-linear, they are analytically not tractable. Instead we use the relaxation method for boundary-value problems, where we replace the ordinary differential equations by a set of equivalent finite-difference equations on a grid of  $M$  points. The origin of the grid is either the monolayer edge or the center of the  $\pi$ -wall, and the final boundary is taken to be large enough to ensure that all derivatives in Eqs. (7)–(14) vanish, and all boundary conditions in the bulk of the Sm- $A^*$  membranes are satisfied. Starting from an initial guess, the algorithm iterates the solution by using Newton's method until the generated numerical values of the dependent variables converge to the true solution up to a relative error [28]. In our implementation each of the two adjacent points on the grid are coupled,  $M = 800$ , and the relative error is in the order of  $10^{-8}$ . The dependent variables to be simultaneously solved in our analysis are  $\theta, \Psi, t, \phi, \mu, \theta', \Psi'$ , and  $\kappa_c$ .

When solving differential equations, it is suitable to work with dimensionless parameters. In our analysis, we use the assumption  $t_0 = \lambda_t$ . The half-length of the  $fd - wt$  viruses are  $t_0 = 0.44 \mu\text{m}$  [30], and from previous theories  $\lambda_t = 0.48 \mu\text{m}$  [10]. In what follows, we will show that this assumption still holds. Furthermore, for simplicity we assume that  $r = C_2$ . Hence, using the previous definitions of  $\lambda_t \equiv \sqrt{\frac{K_2}{C_2 \Psi_0^2}}$ ,  $\Psi_0 \equiv \sqrt{\frac{\tau}{u}}$ , and measuring the distance from the monolayer edge and the  $\pi$ -wall in units of  $\lambda_t$ , we define the following dimensionless constants:

$$\xi_{||} \equiv \sqrt{\frac{C_1}{r}}, \quad \kappa_2 \equiv \frac{\lambda_t}{\xi_{||}}, \quad \alpha \equiv \sqrt{\frac{C_t t_0^4}{r}},$$

$$\bar{\sigma}_{||} \equiv \frac{\sigma_{||} \lambda_t}{K_2}, \quad \bar{\sigma}_{\perp} \equiv \frac{\sigma_{\perp} \lambda_t}{K_2}, \quad \bar{\Delta} \equiv \frac{\Delta \lambda_t}{K_2}, \quad \bar{k} \equiv \frac{k}{K_2 \lambda_t}, \quad (21)$$

$$\bar{\nu} \equiv \frac{\nu \lambda_t^2}{K_2} = -\frac{1}{4} + \frac{(q_0 \lambda_t)^2}{2}. \quad (22)$$

$\xi_{||}$  is the coherence length, and  $\kappa_2$  the twist Ginzburg parameter [2], which is analogous to the Ginzburg parameter  $\kappa$  in superconductors [5, 14].  $\alpha$  is the dimensionless coupling strength of the thickness  $t$  with the projected height of a tilted rod,  $t_0 \cos \theta$ , in the Sm- $A^*$  region. The remaining definitions denoted with bars are the corresponding dimensionless constants.  $q_0 \lambda_t$  in Eq. (22) is the dimensionless chirality of the rods. Using the definitions given by the Eqs. (21), (22) in Eqs. (4) and (5), the dimensionless free energy per unit length  $\bar{F}$  is obtained as  $\bar{F} \equiv F/K_2$ . The dimensionless critical chirality is found as  $q_{0c} \lambda_t = 1/\sqrt{2}$  [2].

The theoretical retardance profile is calculated by plugging the  $t$  and  $\theta$  profiles in Eq. (1). To successfully reproduce the retardance data using the model in Eq. (2), the finite resolution of an object viewed with optical microscopy must be taken into account. The resolution is

characterized by a Gaussian distribution function, and it is convolved with the theoretical retardance to compare the resulting profile with the experimental retardance data [10]. For best fit, the rod concentration  $c$  in Eq. (1) and  $\lambda_t$  are adjusted accordingly. Since the  $\pi$ -wall thickness  $t_{\pi}$  is not determined by experiments, it is a fitting parameter as well. We extract  $t_{\pi}$  from the local minimum of the retardance at the  $\pi$ -wall (Figs. 2e, 6d).

To compare with the line tension measured in experiments, the  $T$ -dependence of  $q_0$  allows us to calculate  $\gamma_{eff}$ , given in Eq. (16), as a function of the temperature (Fig. 7). At approximately  $T_c = 60$  °C wild-type  $fd$  viruses become achiral [11]. Hence  $\gamma_{chiral}$  vanishes in Eq. (16), leading to  $\gamma_{eff} = \gamma_{bare}$ . Beyond this critical temperature  $T_c$  the experimental line tension shows no temperature dependence. The chirality of wild-type  $fd$  viruses was converted into a temperature-dependent function, given by  $q_0 = a(T_c - T)^{1/2}$ , where  $a = 0.056(^{\circ}\text{C} \mu\text{m}^2)^{-1/2}$  [11]. Since self assembly of the rods into the monolayers is primarily governed by hard-core repulsions among the rods and the surrounding depletant, we assume that all other constants in Eqs. (2) and (3) are independent of temperature.

## B. The edge and $\pi$ -wall profiles

Figs. 4–7 display our main results. For convenience, in Figs. 4 and 5 we illustrate the results in terms of dimensionless parameters. The smectic order parameter  $\Psi$ , the thickness  $t$ , and the tilt angle  $\theta$  are calculated as a function of the following dimensionless parameters: the chirality  $q_0 \lambda_t$ , the twist Ginzburg parameter  $\kappa_2$ , the bulk surface tension modulus  $\bar{\sigma}_{||}$ , the surface tension anisotropy  $\bar{\Delta}$ , the thickness coupling strength  $\alpha$ , and the curvature modulus  $\bar{k}$ .

In Fig. 4 the evolution of  $\Psi$ ,  $t$ , and  $\theta$ , versus the distance from the edge, are shown as  $q_0 \lambda_t$ ,  $\bar{\Delta}$ ,  $\bar{k}$ , and  $\alpha$  are varied in successive columns, respectively. The set of these parameters is given in Fig. 4 caption, and all other parameters for a given column are taken to be constant. These constant parameters are;  $q_0 \lambda_t = q_{0c} \lambda_t = 1/\sqrt{2}$ ,  $\kappa_2 = 10$ ,  $\bar{\sigma}_{||} = 0.4$ ,  $\bar{\Delta} = 0$ ,  $\alpha = 15$ , and  $\bar{k} = 0.2$ . To our knowledge, the critical chirality  $q_{0c} \lambda_t$  does not have any thermodynamic significance for Sm- $A^*$  monolayers. However,  $q_{0c} \lambda_t$  is fairly high compared to the range of  $q_0 \lambda_t$  observed in experiments which is approximately between  $q_0 \lambda_t \sim 0 - 0.22$  [11]. Therefore a high value of  $q_0 \lambda_t$  allows us to better examine the effects of the  $Ch$  band formation to the edge structure. The effect of  $\kappa_2$  and  $\bar{\sigma}_{||}$  on the edge structure is found to be negligible. Thus, the evolution of the profiles with respect to  $\kappa_2$  and  $\bar{\sigma}_{||}$  are not shown. From Eq. (21) the energy scale of the surface tension moduli is estimated as  $K_2/\lambda_t \sim 250 k_B T / \mu\text{m}^2$ , given that  $\lambda_t \sim 0.5 \mu\text{m}$  and  $K_2 = 125 \frac{k_B T}{\mu\text{m}}$  [10, 29]. This order of magnitude agrees well with the results presented in Ref. [7]. Therefore we choose the bulk surface tension modulus to be  $\bar{\sigma}_{||} = 0.4$  (on the order of  $10^2 \frac{k_B T}{\mu\text{m}^2}$ ) and

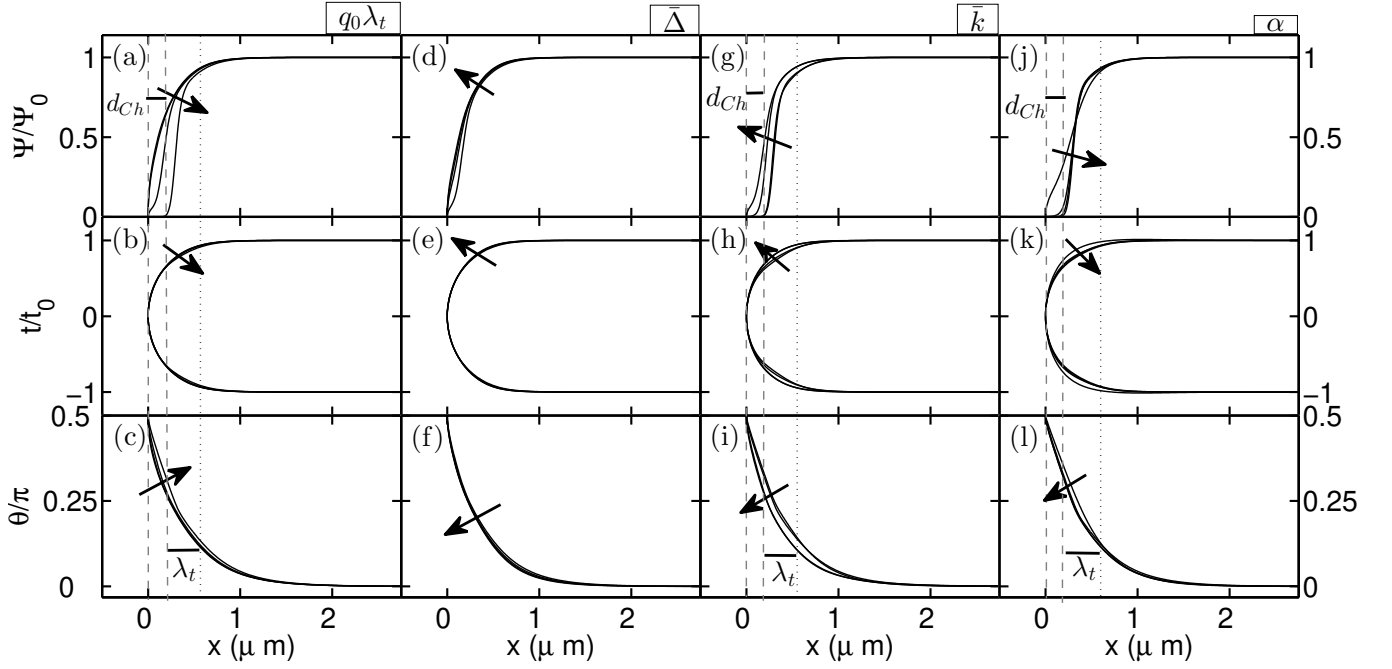


FIG. 4. **From top to bottom, the profiles of the smectic order parameter  $\Psi$ , thickness  $t$ , and the tilt angle  $\theta$ , as a function of the distance from the edge.**  $\Psi$  is normalized by  $\Psi_0 \equiv \sqrt{\frac{\pi}{u}}$ ,  $t$  by  $t_0 = \lambda_t$ , and  $\theta$  by  $\pi$  (vertical axes). The origin of the horizontal axes lie at the monolayer edge, positive values of the distance are inside the monolayer. From left to right, each column displays the evolution of the profiles upon variation of the corresponding dimensionless variable; the chirality  $q_0\lambda_t = \{0, 0.3, 0.6, 1/\sqrt{2}\}$ , the surface tension anisotropy  $\bar{\Delta} = \{0.1, 0.2, 0.3, 0.4\}$ , the curvature modulus  $\bar{k} = \{0.1, 0.2, 0.5, 1.0\}$ , and the thickness coupling strength  $\alpha = \{1, 5, 10, 15\}$ , respectively (Eq. (21)), as denoted at the top. All other parameters are taken to be constant for each column. The arrows are oriented in the direction in which the profiles evolve as the corresponding dimensionless variable increases. In the first, third, and fourth columns, maximum width of the  $Ch$  band  $d_{Ch}$  and corresponding twist penetration depth  $\lambda_t$  are shown.  $\Psi$  exhibits  $Ch$  region,  $t$  qualitatively reproduces the curved shape in the electron micrograph (Fig. 1b), and  $\theta$  shows a decay characterizing the twist penetration at the edge [10]. Overall the profiles are fairly robust upon change of the variables in Eq. (2).

assume the surface tension to be isotropic, that is  $\bar{\Delta} = 0$ .  $\alpha$  and  $\bar{k}$  are not determined by experiments. We set  $\alpha = 15$  to work in the strong-coupling limit. Additionally, we find that  $k \sim k_B T$  or  $10k_B T$  results in  $t$  profiles which qualitatively reproduce the shape of the edge as in Fig. 1(d). This corresponds to a range of  $\bar{k} \sim 0.02 - 0.2$ .

Length scales play a crucial role in understanding the effects of the dimensionless constants on the profiles. By definition,  $\lambda_t$  is measured inside the  $Sm-A^*$  region. That is, the width of the cholesteric band, which we define as  $d_{Ch}$ , does *not* contribute to  $\lambda_t$  (see Figs. 4 and 5).

Figs. 4(a)-(c) show the evolution of the profiles from the achiral limit ( $q_0\lambda_t = 0$ ) to  $q\lambda_t = 1/\sqrt{2}$ . The reduction in the chiral energy density  $-K_2 q_0 \mathbf{n} \cdot (\nabla \times \mathbf{n})$ , given by the cross-term in Eq. (3), favors  $d_{Ch}$  to become bigger when  $q_0\lambda_t$  increases. This is also evidenced by the linear  $\theta$  profiles. In the  $Ch$  phase the last term in Eq. (4) is minimized when  $\mathbf{n} \cdot (\nabla \times \mathbf{n}) = q_0$ , leading to a linear  $\theta$  profile, which corresponds to a uniform twist about a helical axis throughout the sample. The change

in  $t$  profiles is negligible, that is  $q_0\lambda_t$  does not affect the overall shape of the monolayer edge. The twist penetration depth is constant at  $\lambda_t = 0.38 \mu\text{m}$  throughout the whole range of  $q\lambda_t$ . Likewise, in Ref. [11] it is reported that the retardance profiles and  $\lambda_t$  are independent of the molecular chirality  $q_0$ .

In Figs. 4(d)-(f), the effect of anisotropy in the surface tension ( $\Delta > 0$ ) is investigated. When anisotropy increases,  $\theta$  profiles become more steep to suppress the effect of anisotropy, which is given by the fifth term in Eq. (2). Accordingly  $\Psi$  profiles show that  $d_{Ch}$  decreases. Again, the shape of the monolayer edge is not affected, as evidenced by the  $t$  profiles. The change in  $\lambda_t$  is small;  $\lambda_t = 0.39 \mu\text{m}$  for  $\bar{\Delta} = 0.1$  and  $\lambda_t = 0.42 \mu\text{m}$  for  $\bar{\Delta} = 0.4$ .

Figs. 4(g)-(i) indicate that  $\bar{k}$  has a profound effect on the shape and structure of the membrane edge. With increasing  $\bar{k}$ , the apices of  $t$  profiles become flatter. Since we work in the strong coupling limit ( $\alpha = 15$ ), the change in  $\bar{k}$  affects both  $\theta$  and  $\Psi$  profiles.  $d_{Ch}$  becomes lower and  $\theta$  profiles drift apart from the linear regime close to the

edge.  $\bar{k}$  significantly alters the twist penetration depth:  $\lambda_t = 0.34 \mu\text{m}$  when  $\bar{k} = 0.1$  and  $\lambda_t = 0.47 \mu\text{m}$  when  $\bar{k} = 1$ .

The effect of the dimensionless coupling constant  $\alpha$  is examined in Figs. 4(j)-(l). As  $\alpha$  increases, the apices of  $t$  profiles become rounder.  $\theta$  profiles slightly change such that the twist penetration depth grows from  $\lambda_t = 0.34 \mu\text{m}$  for  $\alpha = 1$  to  $\lambda_t = 0.38 \mu\text{m}$  at  $\alpha = 15$ . Additionally,  $d_{Ch}$  becomes bigger when  $\alpha$  increases. When  $\alpha$  is small, there is a deviation between the projected height of the rod  $t_0 \cos \theta$  and  $t$  in the Sm- $A^*$  region. On the other hand, bigger values of  $\alpha$  result in good agreement between  $t$  and  $t_0 \cos \theta$  outside  $d_{Ch}$ . Hence, our choice to work in the strong coupling limit is justified within the framework of our model.

In Fig. 5 the evolution of  $\Psi$ ,  $t$ , and  $\theta$ , versus the distance from the edge, are shown as  $q_0 \lambda_t$ ,  $\kappa_2$ ,  $\bar{k}$ , and  $\alpha$  are varied in successive columns, respectively. Again, all other parameters for each column are taken to be constant. These constant parameters are the same as before, except that  $\bar{k} = 0.05$ , that is,  $k \sim 3k_B T$ . In contrast to the edge structure,  $\pi$ -walls are affected by the anisotropy  $\bar{\Delta}$  negligibly. Therefore, the evolution of the profiles with respect to  $\bar{\Delta}$  will not be discussed. Overall the profiles are very robust upon change of the variables in Eq. (2). For all columns except the column of  $\bar{k}$ , we extract  $\lambda_t = 0.21 \mu\text{m}$ , which is fairly low compared to  $\lambda_t$  of the edge, being independent of  $q_0 \lambda_t$ . Namely the twist penetration depth is constant, as observed in experiments [11].

The change in  $q_0 \lambda_t$  (Figs. 5(a)-(c)) and  $\alpha$  (Figs. 5(j)-(l)) alter the profiles the same way as described above for the edge. However, the effects of  $\kappa_2$  and  $\bar{k}$  on  $\pi$ -wall profiles are qualitatively different from the edge profiles. In Figs. 5(d)-(f), when  $\kappa_2$  changes, the relaxation length scale  $\xi_{||}$  of the smectic order affects  $\Psi$  profiles. As a result,  $d_{Ch}$  becomes bigger for higher  $\kappa_2$ , corresponding to smaller  $\xi_{||}$ , thereby rapid variation of  $\Psi$ . Moreover, Fig. 5(g)-(i) indicate that  $\bar{k}$  has a negligible effect on the shape and structure of the  $\pi$ -wall.  $\lambda_t = 0.23 \mu\text{m}$  (see Fig. 5(i)) for  $\bar{k} = 0.01$  and it reduces to  $0.2 \mu\text{m}$  when  $\bar{k} = 0.1$ .

### C. The retardance and the line tension

Next we interpret the retardance profiles in Figs. 6(d) and (h), calculated from the  $t$  and  $\theta$  profiles displayed in Figs. 6(b)-(c) and (f)-(g). These profiles are obtained for the range of chirality  $q_0 \sim 0 - 0.5 \mu\text{m}^{-1}$  (equivalently  $T \sim 0 - 60 \text{ }^\circ\text{C}$ ) at the strong coupling limit ( $\alpha = 18$ ), corresponding to a depletant concentration of  $35 \text{ mg/mL}$ , as given in Tables I and II. For both types of interfaces, Fig. 6 contains three sets of indistinguishable theoretical profiles (black full curves) corresponding to intermediate and high chiralities within this range, and the achiral limit. That is, the retardance profiles are essentially unchanged, revealing that the  $\pi$ -wall and the edge structures are independent of the rod chirality [11]. The local

minimum of the  $\pi$ -wall retardance is successfully reproduced by our model and allows us to extract the  $\pi$ -wall thickness as  $t_\pi = t_0/4$  (Fig. 6(d)). In the experimentally realized range of  $q_0$ ,  $\Psi$  profiles reveal that the width of the  $Ch$  band goes to zero (Figs. 6(a) and (e)). Furthermore,  $\lambda_t$  is found to be bigger at the edge than at the  $\pi$ -wall (see Tables I, II). We have no simple physical reason for this difference. Revisiting our assumption that  $t_0 = \lambda_t$ , for the edge and the  $\pi$ -walls, we obtain the membrane thickness of  $t_0 \simeq 0.6 \mu\text{m}$  and  $t_0 \simeq 0.8 \mu\text{m}$ , respectively. These results are in reasonable agreement with the expected membrane thickness of  $0.88 \mu\text{m}$ , ignoring protrusion fluctuations of the rods.

Dextran ( $\frac{\text{mg}}{\text{mL}}$ )	$\sigma_{  }(\frac{k_B T}{(\mu\text{m})^2})$	$\sigma_{\perp}(\frac{k_B T}{(\mu\text{m})^2})$	$k(k_B T)$	$\lambda_t(\mu\text{m})$
45	183	349	23.5	0.47
40	145	276	5.38	0.43
35	80	128	4.88	0.39

TABLE I. For the edge,  $\lambda_t$ , surface tension and curvature moduli as a function of the depletant concentration. The twist elastic constant is kept fixed at  $K_2=125 k_B T/\mu\text{m}$  [29]. The twist Ginzburg parameter is chosen as  $\kappa_2 = 4$ . Using Eq. (1), the rod concentration is found to be  $c = 170 \text{ mg/mL}$ .

Dextran ( $\frac{\text{mg}}{\text{mL}}$ )	$\sigma_{  }(\frac{k_B T}{(\mu\text{m})^2})$	$\sigma_{\perp}(\frac{k_B T}{(\mu\text{m})^2})$	$k(k_B T)$	$\lambda_t(\mu\text{m})$
45	184	350	2.13	0.34
40	161	282	1.94	0.31
35	112	179	1.75	0.28

TABLE II. For the  $\pi$ -walls,  $\lambda_t$ , surface tension and curvature moduli as a function of depletant concentration ( $K_2=125 k_B T/\mu\text{m}$ ,  $\kappa_2 = 4$ , and  $c = 145 \text{ mg/mL}$ ).

Eq. (16) states that the chirality of the constituent rods controls the line tensions  $\gamma_{edge}$  and  $\gamma_\pi$ . It follows that decreasing the temperature results in higher chirality of wild-type  $fd$  virus, subsequently reducing  $\gamma_{edge}$  and  $\gamma_\pi$  (Fig. 7), since the twist deformations favored by the edge and  $\pi$ -wall structures also satisfy the chiral interactions. This is realized in Figs. 7(a)-(c). Furthermore, the depletant concentration  $C_{dextran}$  affects the order of magnitude of the line tension. Consequently, when  $C_{dextran}$  decreases from Figs. 7(a) to (c), the overall line tension becomes smaller.

In Fig. 7 the theoretical  $\gamma_{edge}$  (black full curves) and  $\gamma_\pi$  (gray full curves) are compared to the experiments (respectively, black dots and gray squares) as well. For the  $\pi$ -walls we obtain excellent agreement between theory and experiment over the entire range of temperature and depletant concentration. Chirality lowers  $\gamma_\pi$  by up to  $100 k_B T/\mu\text{m}$ . On the other hand, even though the low  $q_0$  behavior and order of magnitude of theoretical  $\gamma_{edge}$  agrees well with experiment, the slopes of the experimental and theoretical  $\gamma_{edge}$  disagree. The origin of this discrepancy, as well as the slope difference between  $\gamma_{edge}$  and  $\gamma_\pi$  are not understood. Additionally, the theoretical line tension profiles of both structures are found

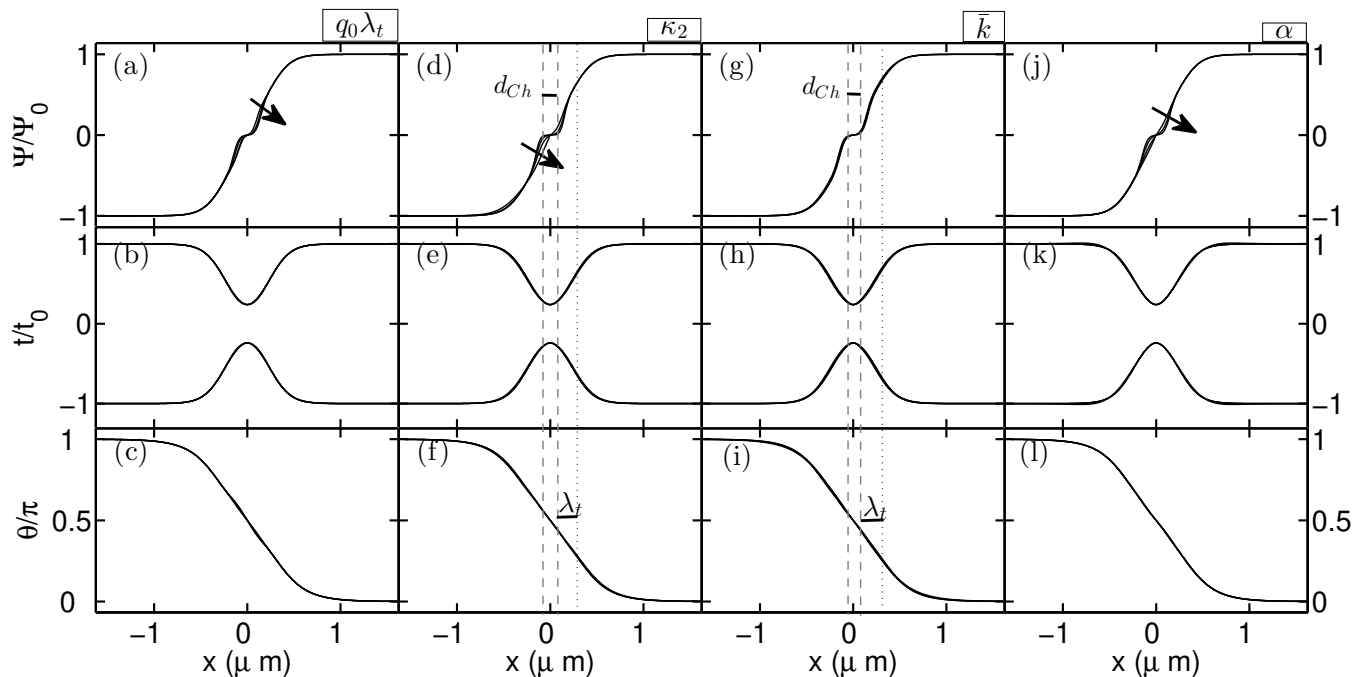


FIG. 5. **From top to bottom, the profiles of the smectic order parameter  $\Psi$ , thickness  $t$ , and the tilt angle  $\theta$ , as a function of the distance from the  $\pi$ -wall.** The origin of the horizontal axes lie at the  $\pi$ -wall, positive and negative values of the distance are inside the monolayer in opposite directions. From left to right, each column displays the evolution of the profiles as a function of the dimensionless variables; the chirality  $q_0\lambda_t = \{0.1, 0.3, 0.6, 1/\sqrt{2}\}$ , the twist Ginzburg parameter  $\kappa_2 = \{2, 6, 10, 15\}$ , the curvature modulus  $\bar{k} = \{0.01, 0.02, 0.05, 0.1\}$ , and the thickness coupling strength  $\alpha = \{1, 5, 10, 15\}$ , respectively (Eq. (21)), as denoted at the top. The arrows are oriented in the direction in which the profiles evolve as the corresponding dimensionless variable increases. In the second and third columns, maximum  $d_{Ch}$  and corresponding  $\lambda_t$  are shown.  $\Psi$  exhibits the  $Ch$  region across the  $\pi$ -wall, and  $\theta$  shows a decay characterizing the twist penetration around the  $\pi$ -wall [10].  $t$  is significantly reduced from  $t_0$  in the bulk to  $t_0/4$  at the center of the  $\pi$ -wall.

to be close to parallel to each other. In contrast to the theory where the reduction is by up to  $100 k_B T / \mu\text{m}$ , chirality reduces  $\gamma_{edge}$  by e.g. up to  $400 k_B T / \mu\text{m}$  when  $C_{dextran} = 45 \text{ mg/mL}$  in experiments (Fig. 7a).

The moduli  $\sigma_{\parallel}$ ,  $\sigma_{\perp}$ , and  $k$  for the theoretical curves in Fig. 7 are given in Tables I and II corresponding to the monolayer edge and the  $\pi$ -wall, respectively, as a function of the depletant concentration. The magnitudes of  $\sigma_{\parallel}$  and  $\sigma_{\perp}$  of both structures are found to be very close to each other, reflecting the unified nature of our model. Besides, their orders of magnitude match with experimental predictions [7]. Whereas the curvature modulus  $k$  is on the order of  $k_B T$  for the  $\pi$ -wall, thermal fluctuations should not alter its shape, since the shape dependence on  $k$  was found to be negligible (Figs 5(g)-(i)). For the edge, although  $k$  affects the structure (see Figs. 4(g)-(i)), the shape qualitatively agrees with the electron micrograph (Fig. 4(e)) for the entire range of  $k$ . Last, in order to fit the slope of  $\gamma_{edge}$  to experiments, an extensive scan over the parameter space resulted in  $\gamma_{edge}$  profiles of similar slopes, solely affecting their magnitude.

Using Eq. (17), we extract the dependence of the con-

tact angle  $\beta_c$  on the experimental profiles of  $\gamma_{edge}$  and  $\gamma_{\pi}$ . At  $\beta_c = \pi$ ,  $\Delta F$  vanishes (Eq. (20)). Thus, at  $T_c$  (the vertical dashed lines in Fig. 7), which corresponds to  $\beta_c = \pi$ ,  $\pi$ -walls should be separated continuously into two free edges and become unstable below  $T_c$ . Furthermore, when  $T$  approaches  $T_c$  from above, a gradual contraction of the  $\pi$ -wall length is expected. None of these predictions are encountered in experiments, and  $\pi$ -walls are observed at temperatures as low as  $T = 5^\circ\text{C}$  (see Fig. 7). This fact may be related with the underlying 3D structure of the anchor points terminating the  $\pi$ -walls. In fact, because of their geometry and liquid crystalline order, anchor points may resist the change in  $\beta_c$  and hence the contraction of the  $\pi$ -wall. Detailed images reveal that these anchors form complex shapes, which are likely to be non-orientable surfaces [12]. Therefore, we conclude that  $\pi$ -walls survive, however become metastable at sufficiently low temperatures. In addition, we exclude the possibility of spontaneous formation of the  $\pi$ -walls at sufficiently high chirality, or equivalently at low temperatures.

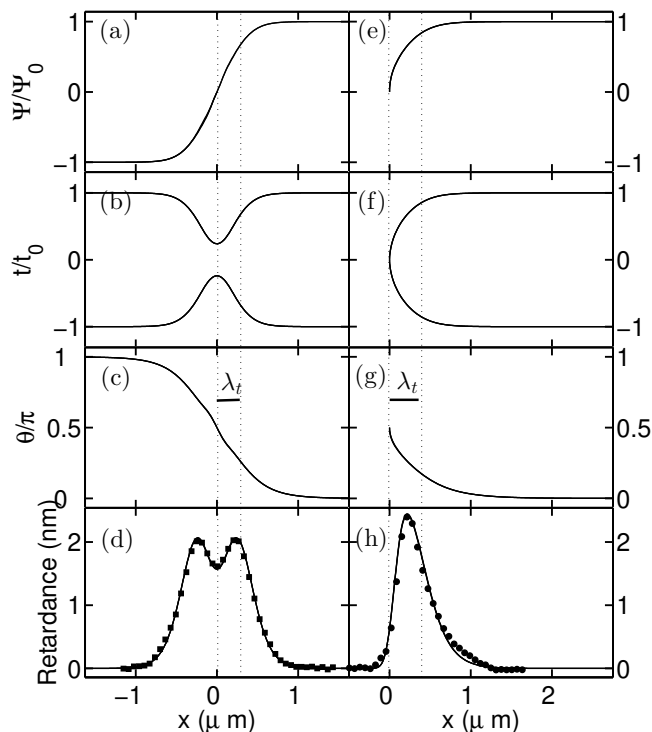


FIG. 6. **Experimental versus theoretical retardance.** From top to bottom, the profiles of the smectic order parameter  $\Psi$ , thickness  $t$ , the tilt angle  $\theta$ , and the retardance  $R$ , as a function of the distance from the  $\pi$ -wall (left column, (a)–(d)) and the edge (right column, (e)–(h)). The origins of the horizontal axes lie at the  $\pi$ -wall (left) and the edge (right). The dotted vertical lines indicate the region of twist penetration  $\lambda_t$ . The squares in (d) and dots in (h) are experimental retardance data, whereas full curves are calculated from Eqs. (7)–(14). Excellent agreement is obtained between experiment and theory, the theoretical retardance being robust upon the change of  $q_0\lambda_t$  (or equivalently, temperature) [11, 12].

#### IV. CONCLUSION

The present theoretical study demonstrates that, in addition to the spatial change of the molecular tilt, the structure of the membrane edge and  $\pi$ -wall are strongly determined by the crossover between  $\text{Sm-A}^*$  and  $\text{Ch}$  regions, as well as the local thickness change in these structures. The membrane lowers the rod-depletant interfacial energy by a hemi-toroidal curved edge. On the other hand, the local thickness change of the  $\pi$ -wall occurs due to the global constraints imposed by its topology, resulting in a retardance drop at the  $\pi$ -wall. Our theory successfully reproduces this unusual retardance behavior, con-

firmed the hypothesized structure of the  $\pi$ -walls. Furthermore, the  $\pi$ -wall thickness, which is not measured in experiments, is determined by our model.

Our calculations indicate that the  $\pi$ -wall line tension is linear in the chirality of viruses. In contrast, line tension measurements of the edge revealed a quadratic dependence on the rod chirality [11], which is not well under-

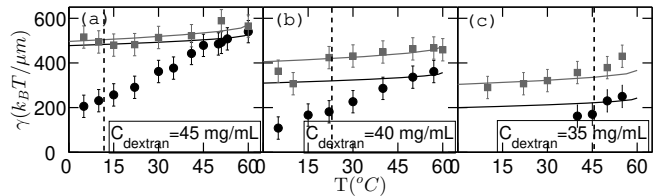


FIG. 7. **The effective line tension  $\gamma$  of both structures as a function of temperature  $T$  and the depletant concentration  $C_{\text{dextran}}$ .** The gray squares and black dots, with their error bars, are extracted from the experimental  $\pi$ -wall and edge fluctuation spectra, respectively [11, 12]. Likewise, the gray and black full curves are the theoretical  $\gamma$  of the  $\pi$ -wall and the edge, respectively, calculated from Eq. (16). The dashed lines correspond  $\beta_c = \pi$ .

stood. A possible explanation is the effect of higher order chiral terms in the Frank elastic theory, as the variation of the molecular director field towards the edge is rapid and may be more significant than around the  $\pi$ -wall.

In the superconductivity literature, the laminar model of alternating normal metal and superconducting regions was abandoned since the Abrikosov vortex lattice phase was found to be more favorable [5, 13, 14]. Nevertheless, its analog in smectics is now realized in the coalescence of  $\text{Sm-A}^*$  monolayers. Note that in the presence of big distortions  $\text{Sm-A}^*$  samples show differences from superconductors, as evidenced by the current study. Hence, the existence of  $\pi$ -walls in bulk  $\text{Sm-A}^*$  samples and their comparison to twist-grain-boundary phases, which are analogous to Abrikosov phases, are subject to further examination.

#### ACKNOWLEDGEMENTS

We thank E. Barry, T. Gibaud, Z. Dogic, R. A. Pelcovits, H. Tu, and M. J. Zakhary for fruitful discussions. This work was supported by the NSF through MRSEC Grant no. 0820492.

[1] M. Schilthuisen and A. Davison, *Naturwissenschaften* **92**, 504 (2005).

[2] S. R. Renn and T. C. Lubensky, *Phys. Rev. A* **38**, 2132 (1988).

- [3] J. W. Goodby, M. A. Waugh, S. M. Stein, E. Chin, R. Pindak, and J. S. Patel, *Nature* **337**, 449 (1989).
- [4] G. Srajer, R. Pindak, M. A. Waugh, J. W. Goodby, and J. S. Patel, *Phys. Rev. Lett.* **64**, 1545 (1990).
- [5] De Gennes, P. G. *Superconductivity of Metals and Alloys* (W.A. Benjamin, 1966).
- [6] P.G. De Gennes, *Solid State Commun.* **10**, 753 (1972).
- [7] E. Barry and Z. Dogic, *PNAS* **107**, 10348 (2010).
- [8] Y. Yang, E. Barry, Z. Dogic, and M.F. Hagan, *Soft Matter* **8**, 707 (2012).
- [9] S. Asakura, F. Oosawa, *J. Polym. Sci.* **33**, 183 (1958).
- [10] E. Barry, Z. Dogic, R.B. Meyer, R.A. Pelcovits, and R. Oldenburg, *J. Phys. Chem B* **113**, 3910 (2009).
- [11] T. Gibaud *et al.* *Nature* **481**, 348 (2012).
- [12] M.J. Zakhary *et al.* *Nat. Commun.* **5**, 3063 (2014).
- [13] B. B. Goodman, *Phys. Rev. Lett.* **6**, 597 (1961).
- [14] Saint-James, D., Thomas, E. J. & Sarma, G. *Type II Superconductivity* (Pergamon Press, 1969).
- [15] R. B. Meyer, *Appl. Phys. Lett.* **12**, 281 (1968).
- [16] P. G. De Gennes, *Solid State Commun.* **6**, 163 (1968).
- [17] F. Bloch, *Z. Phys.* **74**, 295 (1932).
- [18] P.G. De Gennes and J. Prost, *The Physics of Liquid Crystals* (Oxford University Press, 1993).
- [19] K.R. Purdy *et al.* *Phys. Rev. E* **67**, 031708 (2003).
- [20] R.A. Pelcovits and R.B. Meyer, *Liq. Cryst.* **36**, 1157 (2009).
- [21] C.N. Kaplan, H. Tu, R.A. Pelcovits, and R.B. Meyer, *Phys. Rev. E* **81**, 021701 (2010).
- [22] W. Helfrich, *Naturforsch.* **28**, 693 (1973).
- [23] Arfken G., Weber H. *Mathematical Methods for Physicists, Sixth Edition* (Elsevier Inc., 2005).
- [24] E. Barry, D. Beller, and Z. Dogic, *Soft Matter* **5**, 2563 (2009).
- [25] M. Mutz and W. Helfrich, *J. Phys. France* **51**, 991 (1990).
- [26] Y. Yang and M.F. Hagan, *Phys. Rev. E* **84**, 051402 (2011).
- [27] Safran, S. *Statistical Thermodynamics of Surfaces, Interfaces, and Membranes* (Addison Wesley, 1994).
- [28] *Numerical Recipes in C: The Art of Scientific Computing* (1992).
- [29] Z. Dogic and S. Fraden, *Langmuir* **16**, 7820 (2000).
- [30] Z. Dogic and S. Fraden, *Curr. Opin. Colloid Interface Sci.* **11**, 47 (2006).